Physica B 405 (2010) 1501–1508

Contents lists available at ScienceDirect

Physica B

journal homepage: www.elsevier.com/locate/physb

UV optical absorption spectra analysis of beryl crystals from Brazil

Sadao Isotani *, Ana Regina Blak, Shigueo Watanabe

Instituto de Física da Universidade de São Paulo, Cidade Universitária, São Paulo, Brazil

ARTICLE INFO

Article history:
Received 17 June 2009
Received in revised form
16 November 2009
Accepted 9 December 2009

Keywords:
Beryl
Optical absorption
Oxygen vacancy

ABSTRACT

The spectral decomposition analysis was applied to the optical absorption spectra of green and colorless beryl crystals from the Brazilian Eastern Pegmatitic province in the natural state, submitted to heat treatment and irradiated with UV light. The attributions of the lines were made taking into account highly accurate quantum mechanical calculations. The deconvolution of the green beryl spectra revealed four lines, two of them around 12,000 cm^{-1} (1.5 eV) and two of them around 34,000 cm^{-1} (4.2 eV) attributed to Fe^{2+} and Fe^{3+}, respectively. The deconvolution of the colorless beryl spectra without any treatment, after heating and for the same heat treatment followed by UV light irradiation revealed five lines. The analysis of ratio relations showed that the lines at 36,400 cm^{-1} (4.5 eV) and 41,400 cm^{-1} (5.1 eV) belongs to a single defect attributed to a silicon dangling bond defect (═Si:). Discussions and comparison with reported defects in quartz have supported the allocation of the lines at 61,000 cm^{-1} (7.6 eV) and 43,800 cm^{-1} (5.4 eV) to diamagnetic oxygen vacancy defect (═Si–Si═) and unrelaxed (═Si···Si═) defect, respectively. Finally, the line at 39,100 cm^{-1} (4.8 eV), quite polarized along the *c*-axis, was attributed to a ($Fe^{2+}OH^{-}$) defect in the structural channels.

1. Introduction

Beryl is one of the most important gemstones varieties found in the area that includes the Province of Oriental Brazilian Pegmatite in the State of Minas Gerais, Brazil. It constitute an important economical resource of this region and among other gemstones quality crystals were found in pegmatites of the districts Rio das Velhas [1], Araçuai [2], Ponto do Marambaia [3], Volta Grande [4], Mina Cruzeiro [5], Nova Era-Itabira-Ferros [6] and Eastern Brazilian Pegmatite Province as a whole [7,8].

Optical absorption (OA) spectra, in the visible range, were subject of several authors' reports for beryl [9–13], amethyst [14], spodumene [15,16–18], topaz [19–21] and tourmaline [22]. The optical absorption spectra of beryl in the ultraviolet range showed an intensity that increases with energy and has a shoulder very well defined around 40,000 cm^{-1} (5.0 eV) [23]. There are also other lines in the ultraviolet region that were attributed to oxygen vacancies and suggest the presence of OH^{-} ions, in natural beryl, which displaces atomic hydrogen to interstitials [24]. Oxygen vacancies are of fundamental importance in this assumption by allowing the existence of stabilized OH^{-} ions in the structural channels adjacent to the vacancies. The attribution of the optical absorption bands in the UV region to oxygen vacancies was possible to make, based in electron paramagnetic resonance (EPR) and luminescence spectroscopy experimental results associated to highly accurate quantum mechanical calculations [25–27]. These oxygen centers may arise from the irradiation as well as a consequence of thermodynamical equilibrium between the crystal and the surrounding atmosphere [28,29] and are able to give us insights about the kinetics of the natural growth process of these crystals [30].

The EPR measurements of beryl crystals of the Eastern Brazilian Pegmatite Province showed that Fe^{3+} occupies substitutional Al^{3+} sites and also positions in the structural channels between two O_6 planes [9]. OA measurements showed a band at around 12,000 cm^{-1} (1.5 eV) which was attributed to Fe^{2+} in the structural channels. The color change of green beryl to blue beryl was followed by the decrease of the Fe^{3+} EPR band and the increase of the Fe^{2+} OA band. These changes are linearly correlated supporting the change of color attribution to the thermal reduction of Fe^{3+} into Fe^{2+}. The color changes from green to blue was attributed to the OA band shift from 12,100 cm^{-1} to 12,350 cm^{-1} (1.50–1.53 eV). This shift was attributed to Fe^{2+} located at two different sites in the structural channels as assigned by Goldman et al. [31]. The spectral decomposition analysis applied to the band around 12,000 cm^{-1} (1.5 eV) showed that this band is composed by two polarized components, one at 11,750 cm^{-1} (1.46 eV) polarized for the electrical field perpendicular to the *c*-axis and another at 12,750 cm^{-1} (1.58 eV) polarized for the electrical field parallel to the *c*-axis [10]. In these calculations the Fe^{3+} absorption bands in the UV region have not been included.

* Corresponding author. Tel.: +55 11 3091 6805, fax: 55 11 3813 4334.
E-mail address: sisotani@if.usp.br (S. Isotani).

0921-4526/$ - see front matter © 2009 Elsevier B.V. All rights reserved.
doi:10.1016/j.physb.2009.12.029

We report in the present work the spectral decomposition analysis of the OA spectra of green and colorless beryl samples including the UV region. The parameters of these decompositions were refined using the optimization method reported by Isotani and Fujii [32].

2. Samples and experimental details

Beryl ($Be_3Al_2Si_6O_{18}$) is a silicate mineral belonging to the cyclosilicate class. It has a honeycomb-like hexagonal structure and belongs to the P6/mcc space group. The axial parameters are c=9.17 Å and a=9.21 Å [33]. Each ion of Al is surrounded by 6 oxygen atoms located in the vertices of almost regular octahedra. Each octahedral complex AlO_6 is linked to six SiO_4 tetrahedra through common oxygen atoms. The disposition of the octahedra is such that allows the formation of Si_6O_{18} rings. Each beryllium is surrounded by 4 oxygen forming distorted tetrahedra. The Si_6O_{18} rings lay one above the other along the C6 axis forming intercommunicating channels of quite large dimensions. The oxygen that is shared among Si^{4+} ions is an O1 type oxygen and the oxygen that is linked to Al^{3+} and Be^{2+} ions is an O2 type oxygen. Taking into account this configuration, each Si^{4+} ion is surrounded by two O1 oxygens and two O2 oxygens. The diameter of the channels varies from a minimum of 2.8 Å in the plane of the Si_6O_{18} ring and a maximum of 5.1 Å, midway between two neighboring rings. Because of this structure, impurities can be substitutional, interstitial and also located in the channels. In the last case, the water occurs in considerable amounts up to 2.5% in weight without modifying the crystal structure [34]. In Fig. 1 the beryl structural model, using the oxygen framework, is showed to illustrate the above description.

The beryl samples used in the present work were obtained from the Eastern Brazilian Pegmatite Province in the State of Minas Gerais, Brazil and were classified as green beryl and colorless beryl. The samples used in our study were oriented using the external hexagonal morphology and were cut in slices of 0.3–1.0 mm thickness with the c-axis perpendicular to the plane of the slice. They were cut with a diamond saw and polished with pastes first containing chromium oxide, next containing alumina and finally containing diamond.

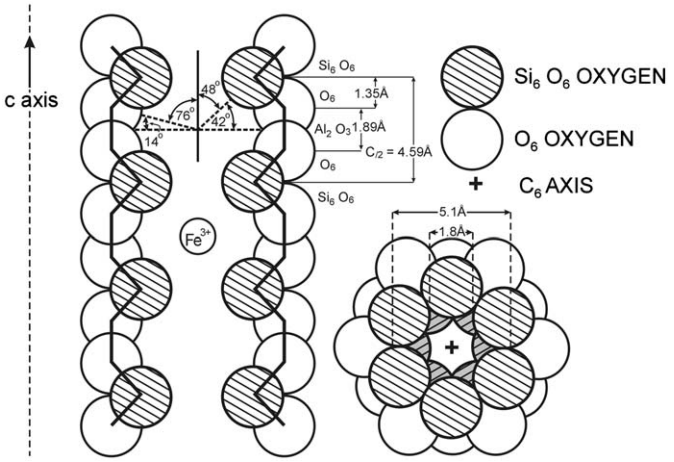

Fig. 1. Schematic drawing showing the Fe^{3+} ion site in the oxygen framework surrounding a channel in the beryl structure. This figure was taken from Ref. [9].

Table 1 presents the values of the impurity concentration obtained through X-ray fluorescence spectroscopy [35] and semi-quantitative atomic emission spectroscopy [23]. These results show that the impurity concentration varies from sample to sample. The measured impurity concentration of the samples used in the present work is similar to the results obtained through semi-quantitative spectrographic analysis and the used criterion was the intensity of the optical transmittance.

The samples were heated in a furnace having a net volume of $10 \times 12 \times 15\,cm^3$ with walls that are filled with refractory bricks. There are also two parallel metallic plates inside it for temperature equilibrium. This arrangement allowed achieving the stability of the furnace with a temperature variation within 1 °C. The temperature inside the furnace was measured with a chromel–alumel thermocouple. Thermal treatments consisted in heating the samples in air.

The samples were irradiated with UV light using a 400 W Hg lamp.

The OA measurements were performed at room temperature using a Carl-Zeiss DMR21 double beam spectrophotometer. One beam passes through the sample holder while the other passes through the reference holder. In our case air was used as reference. This spectrophotometer has a design that minimizes the polarization ray and it has worked satisfactorily in our previous measurements in the visible range [10]. Light beam in the range from 4000 to 30,000 cm^{-1} (0.5–3.7 eV) was produced with a tungsten lamp. Above 30,000 cm^{-1} (3.7 eV) the light beam was produced with a deuterium lamp. A PbS cell was used as a detector in the range of 4000–30,000 cm^{-1} (0.5–1.7 eV). Above 13,500 cm^{-1} (1.7 eV) a photomultiplier was used. The calibration of the spectrophotometer was performed with air as a reference. The opening of the slit is controlled automatically, and if the incident energy is very low opening increases to allow the sign reading and under this condition the intensity increases giving the impression of a band. In our case, in some of the spectra from 47,000 cm^{-1} (5.8 eV) for $\mathbf{k}\perp\mathbf{c}$ and 48,000 cm^{-1} (5.9 eV) for $\mathbf{k}\parallel\mathbf{c}$ a false line was observed and that part with abnormal opening increase was discarded. The spectrum was printed in a special graph paper and the digitalization was done in millimeter units. Therefore, the error used in the determination of the spectra deviations in the digitalization process, was assumed as 1 mm in the spectra deconvolution.

The EPR spectra were obtained with a Varian X-band type spectrometer using TE_{102} rectangular cavities.

3. Spectral decomposition analysis

The OA spectra Gaussian line shape was assumed in modeling the deconvolution at room temperature in this work [15,36]. The

Table 1
Impurities concentration in green and colorless beryl in ppm units where XRFS is the X-ray fluorescence spectroscopy [35] and SQAES the semi-quantitative atomic emission spectroscopy [23].

Sample		Fe	Cr	Mn	V	Mg	Ca	Traces
Green beryl	XRFS	1318 ± 17	143 ± 17	63 ± 12	34 ± 5	–	–	Na, Li
	SQAES	~2300	–	~150	–	~200	~500	Cs, K
Colorless beryl	XRFS	215 ± 13	107 ± 16	111 ± 12	153 ± 5	–	–	Na, Li
	SQAES	~750	–	~150	–	~100	~700	Cs, K

combination of n Gaussians is given by

$$A(\overline{v}) = \sum_{i=1}^{n} \mathbf{a}_i \exp\left[-\left(\frac{\overline{v}-\overline{v}_{oi}}{\Delta\overline{v}_i}\right)\ln 2\right] \quad (1)$$

,where $\overline{v}$, $\overline{v}_{oi}$, $\Delta\overline{v}_i$, and a_i are, respectively, the wave number, the line-position (wave number at the maximum), the line-width, and the amplitude of the i-th component of the spectral line. The area intensity of the assumed Gaussians is directly proportional to the product of the amplitude times the square of the line-widths. Therefore, since the areas of the lines are proportional to the concentration of the absorbents, the best-fitted amplitudes and the best-fitted line intensities are also proportional to the relative concentrations of the absorbents in the sample.

The difficulties of the traditional fitting procedure of Eq. (1) are: the broad lines can hide several Gaussians components, the line-position is outside the experimental measurement range, and also the instability of the equations derived from the best-fit theory. Then, weak ghost lines may arise due to the propagation of errors in the fitting procedure and also from the non-Gaussian behavior introduced by any small problem in the polarization, detector non-linearity or saturation, scattering in the sample surface due to defects in polishing, among others. So, we have done spectral deconvolution using expression (1) and the obtained insight from a previous analysis of spodumene [15] and additional beryl data reported in the cited references as a whole.

After estimating the first values of Eq. (1) parameters, the best fit using these parameters was obtained using the optimization method reported by Isotani and Fujii [32] in the same way as applied to the analysis of the spodumene spectra [15]. This method looks for the best-fit of the parameters through a grid optimization process. In this case, instabilities originated from the best-fit theories which make use of expansions are avoided. Besides this, allows through insights from similar but best resolved spectra, to discard weak ghost lines that may arise from the propagation of errors in the fitting and experimental procedures.

In the comparison among different spectra it is of fundamental importance for the attribution of the lines, the reliability of the determined deviations of the parameters. In the considered best fit procedure of this work, the dispersion of the values was measured for an increase in the cost function of about 20%. The biggest and the smallest values of each parameter were imposed to correspond to 20% of the best fit of the cost function and the error in this parameter was assumed as the biggest difference in relation to that obtained in the best fit.

4. Results

Fig. 2 shows the optical absorption spectrum with **K**∥**c** of natural green beryl, after heating at 600 °C during 5 min and after heating at 600 °C during 40 min. The scale in Fig. 2 is given in absorbance arbitrary units.

The deconvolution of the bands at 12,000 cm^{-1} (1.5 eV) and at 34,000 cm^{-1} (4.2 eV) revealed that they are composed by two lines each, represented by dotted lines in Fig. 2. Table 2 presents the values of the fitting parameters and the respective areas of the lines. The lines attribution will be subject of discussion in the next chapter.

Fig. 3 shows the correlation between the normalized areas of the bands at 12,000 cm^{-1} (1.5 eV) and at 34,000 cm^{-1} (4.2 eV). The band areas were determined through the digitalized spectra numerical integration. The measured areas are directly related to the concentration of Fe^{2+} and Fe^{3+}. The scales in Fig. 3 is given in normalized areas that was obtained by dividing the areas for Fe^{2+} and Fe^{3+} to the values of the respective areas of natural green beryl. This correlation is almost linear showing that the modification that occurs in the bands with the thermal treatment is similar, reinforcing the present attribution of the 34,000 cm^{-1} (4.2 eV) band to Fe^{3+}.

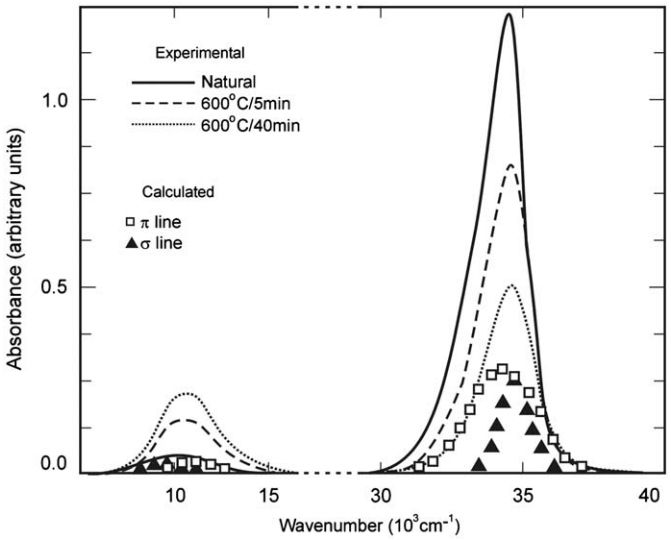

Fig. 2. Optical absorption spectra of natural green beryl, beryl after heating at 600 °C during 5 min and beryl after heating at 600 °C during 40 min. Solid lines are the experimental spectra and traced lines are the fitted lines for natural green beryl.

Fig. 4 shows the optical absorption spectra for **k**||**c** of a natural colorless beryl, after heating at 760 °C during 15 h and for the same heat treatment followed by UV light irradiation during 3 h. The scale in Fig. 4 is given in absorbance arbitrary units. Solid lines are the experimental spectra and the traced lines are the spectrum fitted lines using the fitted parameters presented in Table 2 of beryl after heating at 760 °C during 15 h.

Fig. 5 shows the optical absorption spectra for with **k**⊥**c** of a natural colorless beryl, after heating at 800 °C during 2 h and for the same heat treatment followed by UV light irradiation during 8 h. The scale of the Fig. 5 is given in absorbance arbitrary units. Solid lines are the experimental spectra and the traced lines are the spectrum fitted lines using the fitted parameters presented in Table 2 of beryl after heating at 760 °C during 15 h.

The deconvolution of the thermally treated samples spectra, after the elimination of thermally unstable defects were previously performed. For this purpose we used the same program applied in the deconvolution of the spodumene spectra [15]. The best fitted parameters of the thermally treated samples for **k**∥**c** and **k**⊥**c** are presented in Table 3. We found five lines in the analyzed spectra. There is a large uncertainty in the determination of the energy of the strong absorption in the UV region beyond the measurement range of our spectrophotometer as it was observed in the spodumene spectra analysis. Due to the enormous similarity among the spectra of the present work with those observed in spodumene samples, we adopted as a first fitting option the diamagnetic oxygen vacancy defect (≡Si–Si≡) transition $\mathbf{S_0 \rightarrow S_2}$ around 61,000 cm^{-1} (7.6 eV) for line 5. The best fit deconvolution parameters are presented in Table 3.

Table 4 presents the best fitted parameters of the optical absorption spectra for **k**||**c** and **k**⊥**c** of colorless beryl without any treatment (beryl a). There was no need to introduce new lines for the deconvolution of these spectra. To keep the stability of the process of fitting we introduce a line of very low intensity in 33,500 cm^{-1} (4.15 eV) and line width 1500 cm^{-1} (0.19 eV) for **k**||**c**. It is a bump that occurs because of the presence of the Fe^{3+}.

Table 2
Result of fitting with two Gaussian lines the bands at 12,000 cm^{-1} (1.5 eV) and 34,000 cm^{-1} (4.2 eV).

Sample	Band (cm^{-1})	Attribution	$\overline{\nu}$ (cm^{-1})	$\Delta\overline{\nu}$(cm^{-1})	**a**(au)	a(line σ)/a(line π)
Gb1	12,000	(σ-line)	11.60 ± 0.16	0.80 ± 0.32	9.0 ± 3.7	0.63 ± 0.30
		(π-line)	12.60 ± 0.13	1.10 ± 0.24	14.3 ± 3.3	
	34,000	(σ-line)	34.06 ± 0.06	0.58 ± 0.07	182 ± 22	0.62 ± 0.09
		(π-line)	33.32 ± 0.13	1.27 ± 0.09	293 ± 21	
Gb2	12,000	(σ-line)	11.90 ± 0.16	0.80 ± 0.14	22.85 ± 4.1	0.52 ± 0.11
		(π-line)	12.80 ± 0.25	1.10 ± 0.10	44.0 ± 4.2	
	34,000	(σ-line)	34.22 ± 0.07	0.58 ± 0.11	111 ± 21	0.50 ± 10
		(π-line)	33.60 ± 0.11	1.27 ± 0.11	221 ± 19	
Gb3	12,000	(σ-line)	11.95 ± 0.11	0.80 ± 0.12	28.2 ± 4.3	0.40 ± 0.08
		(π-line)	12.77 ± 0.19	1.10 ± 0.12	70.5 ± 7.8	
	34,000	(σ-line)	34.26 ± 0.14	0.58 ± 0.20	59 ± 20	0.41 ± 0.15
		(π-line)	33.84 ± 0.11	1.27 ± 0.15	145 ± 17	

The samples are green beryl natural (Gb1), heated at 600 °C during 5 min (Gb2) and at 600 °C during 40 min (Gb3). The Gaussian intensities are proportional to the absorbance and are given in arbitrary units (au). The line-position (wave number at maximum) and the line-width are given in units of (10^3 cm^{-1}).

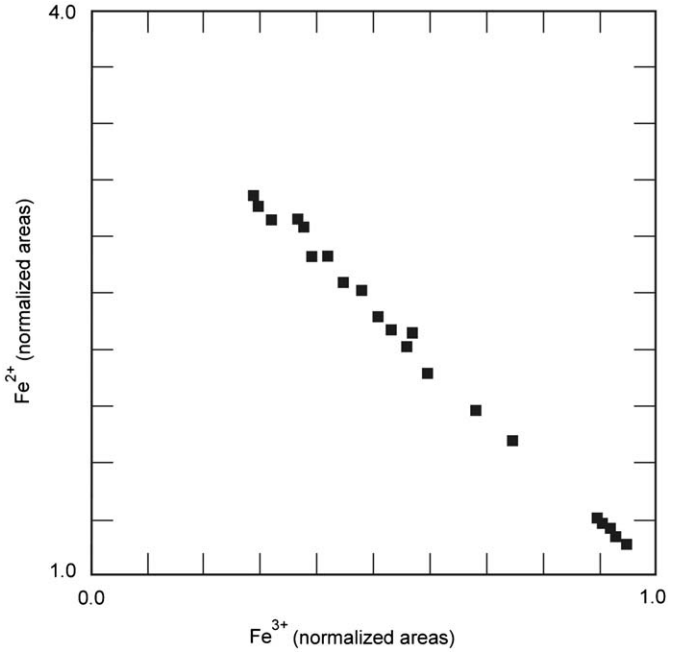

Fig. 3. Correlation between the normalized band areas of Fe^{2+} (12,000 cm^{-1} (1.5 eV)) and Fe^{3+} (34,000 cm^{-1} (4.2 eV)).

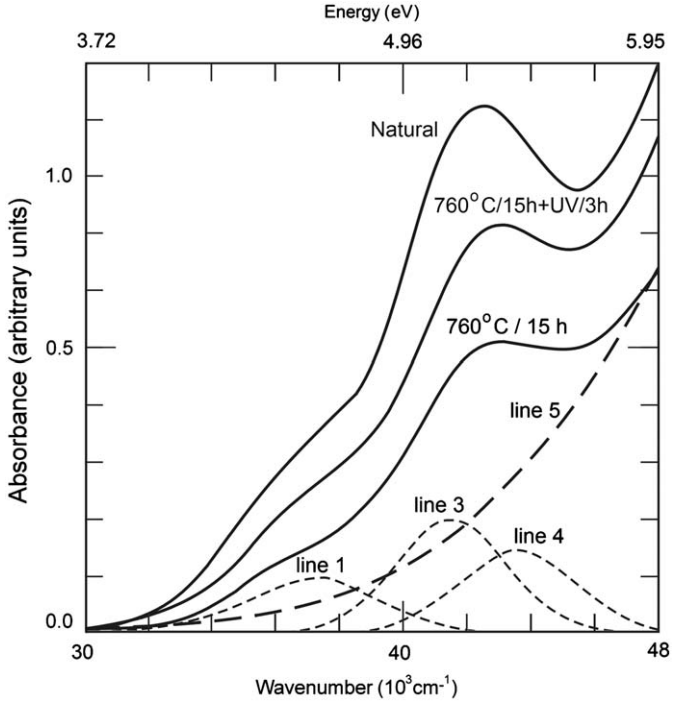

Fig. 4. Optical absorption spectra for **k**∥**c** of natural colorless beryl, after heating at 760 °C during 15 h and for the same heat treatment followed by irradiation with UV light during 3 h. Solid lines are the experimental spectra and traced lines are the fitted lines for beryl after heating at 760 °C during 15 h.

The value of the area of this line is in the region of the fitting error and was not included in this table.

Table 5 presents the best fitted parameters of the optical absorption spectra for **k**∥**c** and **k**⊥**c** of colorless beryl after the thermal treatment followed by UV light irradiation (beryl c). There was no need to introduce new lines for the deconvolution of these spectra. To keep the stability of the fitting process a line of very low intensity at 33,500 cm^{-1} (4.15 eV) and line width 1500 cm^{-1} (0.19 eV) for **k**∥**c** was introduced in the calculation. It is a bump that occurs because of the presence of the Fe^{3+}. The value of the area of this line is in the region of the fitting error and was not included in this table.

The ratios between the areas of the lines together with their errors were calculated from the results presented in Tables 3–5. The ratio between lines 1 and 3 are very similar for both and **k**⊥**c** as it can be seen in Table 6.

In Table 7 we present the ratio between the areas of the lines in relation to the state of them, that is, between lines of the samples a/b and c/b. We find that for the **k**∥**c** direction the ratio decreases in all lines, with special emphasis on line 4. On the other hand in the **k**⊥**c** direction we verify a trend in the opposite direction to what was observed for **k**∥**c**, that is, lines 1–3 increase slightly, and lines 4 and 5 remain nearly constant.

5. Discussion

Fig. 2 shows that the optical absorption spectrum of the green beryl has two asymmetric absorption bands at 12,000 cm^{-1} (1.5 eV) and another one at 34,000 cm^{-1} (4.2 eV). It was shown that the band at 12,000 cm^{-1} (1.5 eV) is composed by two polarized components [9,10]. On the other hand, the composition of the band at 34,000 cm^{-1} (4.2 eV) has not yet been reported as far as we know.

The components of the 12,000 cm^{-1} (1.5 eV) band are a minor energy line denominated σ line and a major energy line

denominated π line. We attributed the fitted line 1 (see Table 2) to the σ line and the fitted line 2 to the π line. The σ line site has been attributed to Fe^{2+} without any neighbor water molecule and the π line to Fe^{2+} with a neighbor type II water molecule (C_2 symmetry axis parallel to the crystal *c*-axis) [9]. Fig. 3 shows a linear correlation between the areas of the band at 12,000 cm^{-1} (1.5 eV) and the band at 34,000 cm^{-1} (4.2 eV). It was also shown that the 12,000 cm^{-1} (1.5 eV) band increase, after heating up the sample above 400 °C, followed by a linearly correlated decay of the Fe^{3+} EPR line located in a beryl channel site. This process was then attributed to the reduction reaction of Fe^{3+} into Fe^{2+}. The observed linear correlation between the increase of the 12,000 cm^{-1} (1.5 eV) OA band and the decay of the 34,000 cm^{-1} (4.2 eV) OA band reinforce the attribution of the 34,000 cm^{-1} (4.2 eV) OA band to Fe^{3+}.

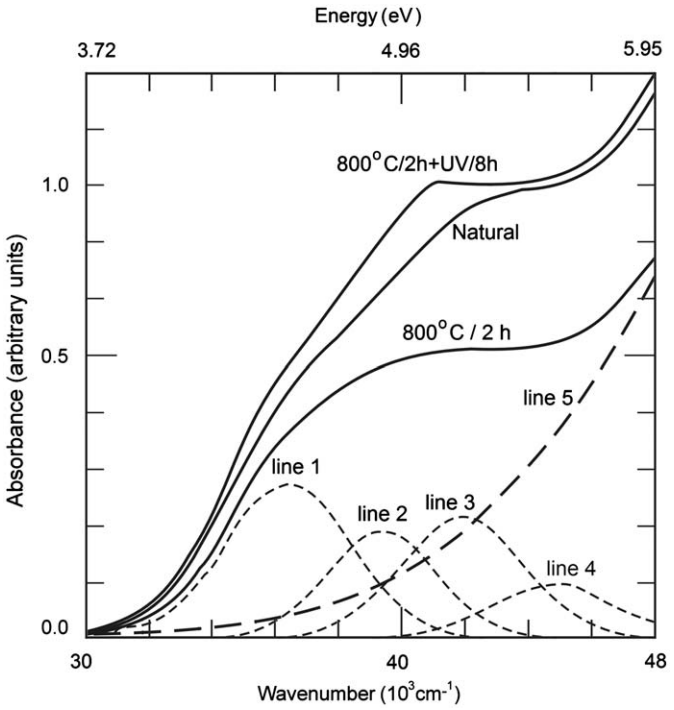

Fig. 5. Optical absorption spectra for **k⊥c** of colorless beryl without any treatment, after heating at 800 °C during 2 h and for the same heat treatment followed by irradiation with UV light during 8 h. Solid lines are the experimental spectra and traced lines are the fitted lines for beryl after heating at 800 °C during 2 h.

From the results presented in Table 2 we see that by heat treatment the π component of the band at 12,000 cm^{-1} (1.5 eV) increases more than the σ component. On the other hand we found that the heat treatment reduces more the component of lower energy of the 34,000 cm^{-1} (4.2 eV) band. Therefore we have attributed the minor energy component of the band at 34,000 cm^{-1} (4.2 eV) to the π-line and the major energy line to the σ-line. Moreover as consequence of these observations the bands at 12,000 cm^{-1} (1.5 eV) and 34,000 cm^{-1} (4.2 eV) undergo a shift in energy towards the blue region during the heat treatment. This blue shift explains the change in color of green beryl to blue after heating.

The absorption spectra of the colorless beryl show an intense absorption in the UV region covering the 34,000 cm^{-1} (4.2 eV) band measured in the green beryl. The spectra of the samples submitted to thermal treatments show a decrease in intensity that is recovered with UV light irradiation. Although the natural samples have not been submitted the any irradiation type we should consider that the beryl crystals were submitted to the background radiation originating from the radioactive impurities contained in the soil [37]. As the samples used for obtaining the spectra were the bulk of the crystals we suggest that the resulting bands, after natural irradiation, are due to defects induced by gamma irradiation. We verified from Fig. 5 that the irradiation with UV light induces a sharp line around 40,000 cm^{-1} (5.0 eV) that is not present in the other analyzed samples showing that beryl has a different response for different types of irradiation.

The following possibilities for the assignment of the absorption lines in the beryl spectrum in the UV region will be taken into account in the discussion: impurity ions, defects in the structure and molecules in the channels.

Table 3
Best fitted parameters of the optical absorption spectra of colorless beryl after thermal treatments.

Peak	**k∥c**			**k⊥c**		
	$\overline{\nu}_{0i}$	$\Delta\overline{\nu}_i$	$\mathbf{a_i}$	$\overline{\nu}_{0i}$	$\Delta\overline{\nu}_i$	$\mathbf{a_i}$
1	37.13 ± 0.06	2.36 ± 0.09	71.5 ± 2.1	36.06 ± 0.04	2.25 ± 0.03	234.9 ± 2.1
2	–	–	–	38.83 ± 0.07	1.94 ± 0.10	141 ± 12
3	41.45 ± 0.04	2.04 ± 0.05	131.3 ± 5.0	41.23 ± 0.10	2.16 ± 0.13	178 ± 17
4	43.54 ± 0.06	2.14 ± 0.05	95.5 ± 1.9	43.98 ± 0.18	2.30 ± 0.21	81 ± 15
5	61.0 ± 0.3	10.5 ± 0.1	6180 ± 240	61.0 ± 0.7	10.5 ± 0.2	8840 ± 880

The Gaussian amplitudes $\mathbf{a_i}$ are proportional to absorbance and are given in arbitrary units, $\overline{\nu}_{0i}$ in 10^3 cm^{-1} and $\Delta\overline{\nu}_i$ in 10^3 cm^{-1}.

Table 4
Best fitted parameters of the optical absorption spectra of colorless natural beryl.

Peak	**k∥c**			**k⊥c**		
	$\overline{\nu}_{0i}$	$\Delta\overline{\nu}_i$	$\mathbf{a_i}$	$\Delta\overline{\nu}_i$	$\Delta\overline{\nu}_i$	$\mathbf{a_i}$
1	36.85 ± 0.06	2.48 ± 0.13	188.5 ± 8.1	36.08 ± 0.03	2.38 ± 0.02	287.0 ± 3.8
2	–	–	–	39.17 ± 0.07	2.15 ± 0.06	193 ± 12
3	41.57 ± 0.04	2.12 ± 0.09	356 ± 19	41.34 ± 0.06	2.18 ± 0.09	200 ± 18
4	43.73 ± 0.09	2.00 ± 0.06	95.5 ± 1.9	43.75 ± 0.06	2.32 ± 0.06	169.8 ± 7.2
5	61.0 ± 0.6	10.5 ± 0.1	9660 ± 920	61.0 ± 0.4	10.5 ± 0.1	12630 ± 730

The Gaussian amplitudes $\mathbf{a_i}$ are proportional to the absorbance and are given in arbitrary units, $\overline{\nu}_{0i}$ in 10^3 cm^{-1} and $\Delta\overline{\nu}_i$ in 10^3 cm^{-1}.

Table 5
Best fitted parameters of the optical absorption spectra of colorless beryl after the thermal treatment followed by irradiation with UV light.

Peak	k∥c			k⊥c		
	$\overline{\nu}_{0i}$	$\Delta\overline{\nu}_i$	$\mathbf{a_i}$	$\overline{\nu}_{0i}$	$\Delta\overline{\nu}_i$	$\mathbf{a_i}$
1	37.21 ± 0.08	2.37 ± 0.17	134.7 ± 7.9	36.12 ± 0.03	2.37 ± 0.02	342.6 ± 3.9
2	–	–	–	39.35 ± 0.08	1.93 ± 0.08	199 ± 21
3	41.87 ± 0.07	2.15 ± 0.05	239 ± 12	41.16 ± 0.20	2.32 ± 0.14	258 ± 28
4	43.80 ± 0.12	1.93 ± 0.09	68.7 ± 2.7	43.78 ± 0.16	2.40 ± 0.13	166 ± 15
5	61.0 ± 0.3	10.5 ± 0.1	8420 ± 520	61.0 ± 0.7	10.5 ± 0.2	13000 ± 1300

The Gaussian amplitudes $\mathbf{a_i}$ are proportional to the absorbance and are given in arbitrary units, $\overline{\nu}_{0i}$ in $10^3\,cm^{-1}$ and $\Delta\overline{\nu}_i$ in $10^3\,cm^{-1}$.

Table 6
Ratio of the best fitted areas of the lines 1 and 3, around $36{,}400\,cm^{-1}$ (4.5 eV) and $41{,}400\,cm^{-1}$ (5.1 eV), for beryl without any treatment, after heating at 760 °C during 15 h and for the same heat treatment followed by UV light irradiation during 3 h.

Sample/(line1/line3)	k∥c	k⊥c
Without any treatment	1.89 ± 0.13	0.767 ± 0.064
After heating	1.84 ± 0.09	0.758 ± 0.073
After heating and UV irradiation	1.77 ± 0.14	0.753 ± 0.082
Mean	1.83 ± 0.07	0.759 ± 0.042

Table 7
Ratio of the best fitted areas of beryl without any treatment (a), after heating at 760 °C during 15 h (b) and for the same heat treatment followed by UV light irradiation during 3 h (c).

Sample orientation	k∥c		K⊥c	
Line/ratio	(a)/(b)	(c)/(b)	(a)/(b)	(c)/(b)
1	2.64 ± 0.14	1.88 ± 0.12	1.22 ± 0.02	1.46 ± 0.02
2	–	–	1.37 ± 0.14	1.45 ± 0.21
3	2.71 ± 0.18	1.80 ± 0.11	1.24 ± 0.16	1.45 ± 0.21
4	1.11 ± 0.04	0.72 ± 0.03	2.10 ± 0.40	2.05 ± 0.42
5	1.56 ± 0.16	1.36 ± 0.10	1.43 ± 0.16	1.47 ± 0.21

The most common impurities in beryl that could provide OA in the UV region are Mn, Ti and Fe. The EPR spectra of pink beryl show traces of Mn^{2+} [23]. The absence of the Mn^{2+} characteristic OA line around $24{,}000\,cm^{-1}$ (3.0 eV) is an indication that the Mn^{2+} concentration is below the detention limit [38]. Thus the Mn^{2+} was discarded in the attribution of the OA bands in the UV region. Ti^{4+} energy transitions of $27{,}000\,cm^{-1}$ (3.3 eV) and $30{,}000\,cm^{-1}$ (3.7 eV) were observed in rutile and anatase, respectively [39]. In the beryl spectra these lines were not found confirming that in beryl, Ti is in insufficient quantities to explain the UV bands.

Since iron has charge transfer lines between $39{,}000\,cm^{-1}$ (4.8 eV) and $45{,}000\,cm^{-1}$ (5.6 eV) in glass [40], it is the best impurity candidate to explain the bands in the UV region. These ions occupy the Si site, then it would be expected to observe optical absorption bands at $6000\,cm^{-1}$ (0.7 eV) and $9000\,cm^{-1}$ (1.1 eV) [17,18]. However, in beryl only bands of Fe^{2+} in the channels [38] at large distances from the oxygen were observed, a factor that inhibits the charge transfer process. The EPR spectra of pink beryl show the presence of manganese and also a line around $g=2$ attributed to Fe^{3+} in the channels of the beryl [23]. The decay of this line was attributed to the reduction of Fe^{3+} into Fe^{2+}. After the thermal treatment there is a considerable reduction of all lines around $g=2$ related to several other paramagnetic defects. In addition almost all paramagnetic defects will not survive heat treatments above 700 °C during a few hours. So the Fe^{2+} ion is a possible candidate to explain one of the lines of the UV band in thermally treated beryl samples with energy around $40{,}000\,cm^{-1}$ (5 eV).

The most common defect in oxides is the oxygen vacancy defect. The Si_6O_{18} rings of beryl lay one above the other along the *c*-axis forming intercommunicating channels of quite large dimensions. Each Al is surrounded by six O2 oxygen ions and each Be is surrounded by four O2 oxygen ions. The presence of the oxygen as linking Si, Al and Be ions, suggests that oxygen defects are the most common defects in beryl. It is well known that thermal treatments up to 800 °C during 15 h destroy the oxygen defects that were created after irradiation. Therefore we consider in the analysis of the heated samples, oxygen vacancy centers. These oxygen centers may arise as a consequence of thermodynamic equilibrium between the crystal and the surrounding atmosphere [28,41]. In beryl there are at least three possible intrinsic oxygen defects. A deficiency of O1 oxygen that is shared by two Si, can produce a defect of oxygen vacancy ($\equiv$Si–Si$\equiv$) type, if it is free to relax. The single oxygen vacancy defect ($\equiv$Si–Si$\equiv$) transition $\mathbf{S_0 \rightarrow S_2}$ in quartz has been reported to be at $63{,}000\,cm^{-1}$ (7.8 eV) [42]. Another possibility takes into account that this defect is on the wall of the channels. Since water molecules are found in great amounts in these channels, the volume occupied by the water prevents the relaxation of the two Si giving rise to an unrelaxed oxygen defect ($\equiv$Si$\cdots$Si$\equiv$). The deficiency of O2 oxygen can produce a silicon dangling bond defect ($=$Si:).

We discard in this work the possibility to attribute to the NBOHC ($16{,}000\,cm^{-1}$ (2.0 eV), $39{,}000\,cm^{-1}$ (4.8 eV) and $55{,}000\,cm^{-1}$ (6.8 eV)) the lines of the UV region because we do not observe the absorption band at $16{,}000\,cm^{-1}$ (2.0 eV) associated with this defect [42–45]. Another argument is that the central band in the EPR spectrum that could be associated with this defect showed a dramatic reduction with the thermal treatment [23]. The assignment of this EPR line in beryl to a Fe^{3+} ion is supported by the correlation studies between the EPR lines and the OA bands [9].

Water molecules very often occupy sites in beryl channels. There are two possible sites in the channels to be occupied. Site I has its C_2 symmetry axis perpendicular to the crystal *c*-axis and site II has its C_2 symmetry axis parallel to the crystal *c*-axis [23]. The IR spectrum of colorless beryl shows that there is a line at $3700\,cm^{-1}$ (0.46 eV) [23], whose energy is slightly higher than the highest energy of type I water [46,47]. Since in the IR spectra of beryl where the hydrogen was replaced by deuterium the energy of the line assigned to OD^- is more energetic than the line that was attributed to water [48], we assign the line at $3700\,cm^{-1}$ (0.46 eV) to OH^- ions. These ions act as charge compensators for alkaline and iron impurities in the channels and probably arise from the water photo-dissociation under irradiation, taking part in defect stability processes [42–45].

In samples submitted to thermal treatments, EPR studies show that the H^0 lines are created in significantly larger quantities than

in natural samples without any treatment. The H^0 high mobility at room temperature suggests the rapid recombination of the centers in unheated samples in the channels due to the large amounts of water. Furthermore, the thermal treatment can reduce the water amount, in a proportion where the rate of H^0 production can overcome the recombination process in the channels and H^0 significant quantities can migrate to beryl interstices. A novel damage mediated by the H^0 migration was reported in quartz assigned to a silicon dangling bond, where the Si atom is bounded by two bridging oxygens and an OH group forming the E′(OH)-center [45].

Taking into account the results obtained from Table 7 of the ratios between the same lines in different samples for several thermal treatments, we conclude that the removal of water in the thermal treated samples modifies the way the defects had been formed. The most striking result of the removal of water from the channels was the recombination reduction of hydrolyzed water, leaving more H^0 and OH^- ions in the channels.

CO_2 molecules are also found in beryl channels, as it can be verified from the IR spectra of green, blue and pink crystals [23,49]. In the IR spectra, a very small line around 3200 cm^{-1} (0.40 eV) is also observed, which has been assigned to ammonia molecules [50]. In appropriate conditions, probably with the presence of neighboring ions, the irradiation produces CO_3^- radicals giving rise to an IR line with sidebands produced by vibronic interactions [38]. Thermal treatments do not affect the IR spectra confirming that CO_2 molecules have low mobility in the channels. Moreover it was observed that the decay kinetics of CO_3^- ion is of first-order. Then, the most likely model for the formation process of this defect would be the dislocation of O1 oxygen after the irradiation, reacting with a neighbor CO_2 molecule giving rise to an unrelaxed oxygen defect (≡Si···Si≡).

Therefore, considering the above discussion we assign line 5 at 61,000 cm − 1 (7.6 eV) to the single oxygen vacancy defect (≡Si–Si≡) corresponding to the transition $\mathbf{S_0}\rightarrow\mathbf{S_2}$. We attribute the different ratios a/b and c/b between the areas for $\mathbf{k}||\mathbf{c}$ and $\mathbf{k}\perp\mathbf{c}$ to the high presence of H^0 and OH^- ions modifying the defect polarizability without changing the transition energy.

Lines 1 and 3 around 36,400 cm^{-1} (4.5 eV) and 41,400 cm^{-1} (5.1 eV) appear in the spectra for $\mathbf{k}\perp\mathbf{c}$ and $\mathbf{k}||\mathbf{c}$. The results of the deconvolution presented in Table 6 revealed that the ratio between the areas of all spectra is similar. Hence these lines were assigned to a single defect. Quantum mechanical calculations TD-DFT for the exchange correlation functional (LDA/6-31+G*), (BLYP/6-31+G*) and (PW91/6-31+G*) allow us to consider two possible options: a peroxy bridge defect (≡Si–O–O–Si≡) with transitions $\mathbf{S_0}\rightarrow\mathbf{S_2}$ at 37,600–37,840 cm^{-1} (4.66–4.69 eV) and $\mathbf{S_0}\rightarrow\mathbf{S_2}$ at 38,900–41,390 cm^{-1} (4.82–5.13 eV), and a silicon dangling bond defect (≡Si:) with transitions $\mathbf{S_0}\rightarrow\mathbf{S_2}$ at 38,330–38,490 cm^{-1} (4.75 – 4.77 eV) and $\mathbf{S_0}\rightarrow\mathbf{S_2}$ at 41,640–41,960 cm^{-1} (5.16–5.20 eV) [3]. Moreover (B3LYP/6-31+G*) gives significantly higher transition energies for the peroxy bridge defect (≡Si–O–O–Si≡) $\mathbf{S_0}\rightarrow\mathbf{S_2}$ at 41,070 cm^{-1} (5.09 eV) and $\mathbf{S_0}\rightarrow\mathbf{S_2}$ at 48,980 cm^{-1} (6.07 eV) and for the silicon dangling bond defect (≡Si:) $\mathbf{S_0}\rightarrow\mathbf{S_2}$ at 42,260 cm^{-1} (4.99 eV) and $\mathbf{S_0}\rightarrow\mathbf{S_2}$ at 47,120 cm^{-1} (5.84 eV). As the transition energy varies with the exchange, we compare the differences between the transition energies. In this case the differences for (LDA/6–31+G*), (BLYP/6-31+G*), (PW91/6–31+G*) and (B3LYP/6–31+G*) between the transitions $\mathbf{S_0}\rightarrow\mathbf{S_2}$ and $\mathbf{S_0}\rightarrow\mathbf{S_2}$ are 3790, 1450, 1210 and 6460 cm^{-1} (0.47, 0.18, 0.15 and 0.98 eV) for the peroxy bridge defect and 3310, 3470, 3390 and 6860 cm^{-1} (0.41, 0.43, 0.42 and 0.85 eV) for the silicon dangling bond defect, respectively. The difference between the transitions $\mathbf{S_0}\rightarrow\mathbf{S_2}$ and $\mathbf{S_0}\rightarrow\mathbf{S_2}$ from the deconvolution process is 4840 cm^{-1} (0.6 eV). On the other hand the theoretical differences for (≡Si≡O) and (≡Si(O2)) defects are 1940–3070 cm^{-1} (0.24–0.38 eV) and 14,120–14,280 cm^{-1} (1.75–1.77 eV), respectively. Then, as a first attempt, we attribute lines 1 and 3 to a silicon dangling bond defect (≡Si:).

Line 4 around 43,800 cm^{-1} (5.4 eV) appear in the spectra for $\mathbf{k}\perp\mathbf{c}$ and $\mathbf{k}||\mathbf{c}$. We discarded the attribution of this line to defects like (≡Si≡O) and (≡Si(O2)) because quantum mechanical calculations showed that there are two transitions in this region of energy. For (≡Si(O2)) the line at 24,200 cm^{-1} (3 eV) was not found [42]. Irradiation with ArF excimer laser in dehydrated high-purity silica glass showed the formation of defects with OA in 61,000 cm^{-1} (7.6 eV) and 40,300 cm^{-1} (5.0 eV) [28,41]. Analysis of thermal treatments in O_2 atmosphere lead to the attribution of the 61,000 cm^{-1} (7.6 eV) line to an oxygen vacancy defect (≡Si–Si≡) and the 40,300 cm^{-1} (5.0 eV) line to an unrelaxed oxygen vacancy defect (≡Si···Si≡). The unrelaxed (≡Si···Si≡) defect is one of the intrinsic defects that are expected in the beryl structure and so we attributed line 4 to this defect.

Line 2 at around 39,100 cm^{-1} (4.8 eV) is a single line quite polarized appearing only for $\mathbf{k}\perp\mathbf{c}$. This fact suggests a defect with a dipole moment parallel to the *c*-axis direction. Since the rings of Si_6O_{18} are arranged along the *c*-axis so that the ions of Si are not aligned along this axis we consider unlikely to assign line 1 to a Si defect. Another possibility is to assign line 2 to a defect associated to Fe^{2+} ions in the channels. X-ray and UV irradiation give rise to H^0 centers due to radiation-induced decomposition of water [51,52]. Since Fe ions can be associated to type II water, irradiation in the neighbor water may produce a ($Fe^{2+}OH^-$) defect. A charge transfer interaction between iron and oxygen may give rise to the 39,500 cm^{-1} (4.9 eV) polarized transition.

6. Conclusion

In this work we applied the analysis of OA spectral decomposition of green and colorless beryl crystals of the Eastern Brazilian Pegmatite Province in natural state, submitted to heat treatment and irradiated with UV light.

The deconvolution of the spectra of blue beryl revealed four lines, two of them around 12,000 cm^{-1} (1.5 eV) and two of them around 34,000 cm^{-1} (4.2 eV). The band at around 12,000 cm^{-1} (1.5 eV) was shown previously to be composed by two polarized components [10]. The σ line was attributed to Fe^{2+} without a neighbor water molecule and the π line to Fe^{2+} with a neighbor type II water molecule (C_2 symmetry axis parallel to the crystal *c*-axis) [9]. Correlation between the relationship among the areas of the two lines of the band at 12,000 cm^{-1} (1.5 eV) and that of the band at 34,000 cm^{-1} (4.2 eV), showed that the minor energy line of the band 34,000 cm^{-1} (4.2 eV) could be attributed to the π line and the major energy line to the σ line. Since the amount of Fe^{2+} increases with the thermal reduction of Fe^{3+} into Fe^{2+} [9,10] the band around 34,000 cm^{-1} (4.2 eV) was attributed to Fe^{3+}.

The deconvolution of colorless beryl spectra without any treatment, after heating and for the same heat treatment followed by UV light irradiation revealed five bands. The ratio relations between the fitted areas of the bands at 36,400 cm^{-1} (4.5 eV) and 41,400 (5.1 eV) cm^{-1} are similar. Then, they were attributed to a single defect. Discussions led to assign these bands to a silicon dangling bond defect (≡Si:). Comparisons with defects observed in quartz, discussions on possible defects and the support of highly accurate quantum mechanical calculations led us to assign the bands at 61,000 cm^{-1} (7.6 eV) and 43,800 cm^{-1} (5.4 eV) to diamagnetic oxygen vacancy defect (≡Si–Si≡) and unrelaxed (≡Si···Si≡) defect, respectively. Finally, a quite polarized band at 39,100 cm^{-1} (4.8 eV) was found. The absence of the OA band at 16,000 cm^{-1} (2.0 eV), the dramatic reduction of the EPR line at

$g \sim 2$ and the reported correlation between EPR and OA bands attributed to the Fe^{3+} reduction into Fe^{2+}, led us to discard the attribution to a NBOHC defect. Then, analyzing the polarization of this band along the *c*-axis, and taking in consideration previous works on water and other impurities in the channels, we attributed the band at 39,100 cm^{-1} (4.8 eV) to the defect ($Fe^{2+}OH^{-}$) in the channels.

Acknowledgments

This work was supported with Grants from FAPESP, RHAE, FINEP and CNPq.

References

[1] N. Machado, A. Schrank, C.M. Noce, G. Gauthier, Earth and Planetary Science Letters 141 (1996) 259.
[2] A.C. Pedrosa-Soares, F. Alkmim, A. Whittington, S. Marshak, The Geologial Society of America Annual Meeting, Boston, Massachusetts, 2001 section 63, November 5–8.
[3] M.S.F. Ferreira, M.A. Fonseca, F.R.M. Pires, Revista Brasileira de Geociências 35 (2005) 463.
[4] M. Lagache, J. Quemeneur, Canadian Mineralogist 35 (1997) 153.
[5] B.L. Dutrow, D.J. Henry, Canadian Mineralogist 38 (2000) 131.
[6] C. Preinfalk, Y. Kostitsyn, G. Morteani, Journal of South American Earth Sciences 14 (2002) 867.
[7] G. Morteani, C. Preinfalk, A.H. Horn, Mineralium Deposita 35 (7) (2000) 638.
[8] R.R. Viana, I. Manttari, H. Kunst, H. Jordt-Evangelista, Journal of South American Earth Sciences 16 (2003) 493.
[9] A.R. Blak, S. Isotani, S. Watanabe, Journal of Physical and Chemistry of Minerals 8 (1982) 161.
[10] S. Isotani, W.W. Furtado, R. Antonini, O.L. Dias, American Mineralogist 74 (1989) 432.
[11] K. Krambrock, M.V.B. Pinheiro, K.J. Guedes, S.M. Medeiros, S. Schweizer, C. Castaneda, N.F. Botelho, A.C. Pedrosa-Soares, Nuclear Instruments and Methods B 191 (2002) 285.
[12] R.R. Viana, H. Jordt-Evangelista, G.M. da Costa, B. Stern, Physics and Chemistry of Minerals 29 (2002) 668.
[13] J.C.R. Mittani, S. Watanabe, J.F.D. Chubaci, M. Matsuoka, D.L. Baptista, F. C Zawislak, Nuclear Instruments and Methods B 191 (2002) 281.
[14] C.T. Dotto, S. Isotani, Radiation Effects and Defects in Solids 117 (1991) 355.
[15] S. Isotani, K. Watari, A. Mizukami, W. Bonventi Jr, A.S. Ito, Physica B 391 (2007) 322.
[16] A.T. Fujii, S. Isotani, Anais da Academia Brasileira de Ciências 60 (1988) 127.
[17] A.S. Ito, S. Isotani, Radiation Effects and Defects in Solids 116 (1991) 307.
[18] S. Isotani, A.T. Fujii, R. Antonini, W.M. Pontuschka, S.R. Rabbani, W.W. Furtado, Anais da Academia Brasileira de Ciências 63 (1991) 127.
[19] K. Nassau, B.E. Prescott, American Mineralogist 60 (1975) 705.
[20] A.R.P.L. Albuquerque, S. Isotani, S.P. Morato, Radiation Effects and Defects in Solids 106 (1988) 143.
[21] V. Priest, D.L. Cowan, D.G. Reichel, F.K. Ross, Journal of Applied Physics 68 (1990) 3035.
[22] M.B. de Camargo, S. Isotani, American Mineralogist 73 (1988) 172.
[23] A.R. Blak, S. Isotani, S. Watanabe, Brazilian Review of Physics 12 (1982) 285.
[24] A.R. Blak, S.W. Mckeever, Radiation Protection Dosimetry 47 (1993) 95.
[25] G. Pacchioni, G. Ieranò, Journal of Non-Crystalline Solids 216 (1997) 1.
[26] K. Raghavachari, D. Ricci, G. Pacchioni, Journal of Chemical Physics 116 (2002) 825.
[27] L. Skuja, M. Mizoguchi, H. Hosono, H. Kawazoe, Nuclear Instruments and Methods in Physics Research B: Beam Interactions with Materials and Atoms 166–167 (2000) 711.
[28] F. Agullo-Lopez, C.R.A. Catlow, P.D. Townsend, Point Defects in Materials, Academic Press, London, 1988.
[29] A.S. Marfunin, Spectroscopy, Luminescence and Radiation Centers in Minerals, Springer, Berlin, Heidelberg, New York, 1979.
[30] P.W. Levy, Thermoluminescence of Geological Materials, Academic Press, London, New York, 1968 25–38.
[31] D.S. Goldman, G.R. Rossman, K.M. Parkin, Physical Chemistry of Minerals 3 (1978) 225.
[32] S. Isotani, A.T. Fujii, Computer Physics Communications 151 (2003) 1.
[33] W.A. Deer, R.A. Howie, I. Zussman, An Introduction to the Rock-Forming Minerals, 2, Longman Group Ltd, London, 1978.
[34] V.G. Feklichev, Geokhimya 4 (1963) 419.
[35] O.L. Dias, A.R.P.L. Albuquerque, S. Isotani, Anais da Academia Brasileira de Ciências 55 (1983) 173.
[36] J.J. Markham, Reviews of Modern Physics 31 (1959) 956.
[37] S. Watanabe, M. Sastry, H.S.L. Sullasi, F. Camargo, P. Poirier, M.M.C. Silva, Nuclear Instruments and Methods in Physics Research, Section B, Beam Interactions with Materials and Atoms 213 (2004) 751.
[38] S. Isotani, A.R.P.L. Albuquerque, O.L. Dias, W.W. Furtado, Anais da Academia Brasileira de Ciências 60 (1988) 393.
[39] A.S. Marfunin, Physics of Minerals and Inorganic Materials, Springer, Berlin, Heidelberg, New York, 1979, pp. 202.
[40] D. Ehrt, Comptes rendue Chimie 5 (2002) 679.
[41] R.E. Howard, A.B. Lidiard, Reports on Progress in Physics 27 (1964) 161.
[42] H. Imai, K. Arai, H. Imagawa, H. Hosono, Y. Abe, Physical Review B 38 (1988) 12772.
[43] H. Hosono, K. Kajihara, T. Suzuki, Y. Ikuta, L. Skuja, M. Hirano, Solid State Communication 122 (2002) 117.
[44] M. Cannas, F.M. Gelardi, Physical Review B 69 (2004) 15320.
[45] L. Skuja, K. Kajihara, M. Hirano, A. Saitoh, H. Hosono, Journal of Non-Crystalline Solids 352 (23–25) (2006) 2297.
[46] D.L. Wood, K. Nassau, Journal of Chemical Physics 47 (1967) 2220.
[47] B. Charoy, P. de Donato, O. Barres, C. Pinto-Coelho, American Mineralogist 81 (1996) 395.
[48] P. de Donato, A. Cheilletz, O. Barres, J. Yvon, Applied Spectroscopy 58 (5) (2004) 521.
[49] C. Vianna, A.R. Blak, Radiation effects and defects 134 (1995) 315.
[50] R.I. Mashkovtsev, V.P. Solntsev, Physics and Chemistry of Minerals 29 (1) (2002) 65.
[51] A.R. Blak, W.M. Pontuschka, S. Isotani, Anais da Academia Brasileira de Ciências 60 (1988) 9.
[52] S. Isotani, W.W. Furtado, R. Antonini, A.R. Blak, W.M. Pontuschka, T. Tome, S.R. Rabbani, Physical Review B 42 (1990) 5966.